Studying invariants of the velocity gradient tensor of a round turbulent jet across the turbulent/nonturbulent interface using Tomo-PIV

Morteza Khashehchi[1], Gerrit E Elsinga[2], Andrew Ooi[1], Julio Soria[3], Ivan Marusic[1]

1: Department of Mechanical Engineering, University of Melbourne, Victoria, 3010, AUSTRALIA, moryk@unimelb.edu.au
2: Laboratory for Aero and Hydrodynamics, Department of Mechanical Engineering, Delft University of Technology, Delft, THE NETHERLANDS
3: Laboratory for Turbulence Research in Aerospace and Combustion, Department of Aerospace and Mechanical Engineering, Monash University, Clayton, Victoria, 3800, AUSTRALIA

Abstract Tomographic Particle Image Velocimetry (Tomo-PIV) methodology was used to study the turbulent/ nonturbulent interface of a free air jet at *Re=3000*. A vorticity thresholding technique was used and found to compare well against available results obtained using a similar detection criterion (Bisset et al. 1998). The joint probability density functions (jpdf) of the invariants of the velocity gradient tensor were also obtained and were used to characterize the dynamics, geometry and topology of the flow in the entrainment process. In general, it is observed that values of the invariants are all zero in the irrotational region and change rapidly when the T/NT interface is crossed. Furthermore, the jpdf of (Q_s, Q_w) shows a sharp tendency toward the Q_s axis at the interface indicating predominance of viscous dissipation in that region. The jpdf of R, Q shows that the universal shape, the so-called "tear drop", is not formed at the interface, but rather only inside the turbulent region. The shape of the jpdf of (R_s, Q_s) is found to be unaffected by the entrainment process. These results are in good agreement with the work of Da-Silva et al. (2008) performed similar analysis on DNS data.

1. Introduction

The distinction between a turbulent shear flow and a non-turbulent environment has been a flow feature of great interest due to the inhomogeneity in the flow field responsible for transferring heat, mass and momentum into the turbulent region. The dynamics of this sharp and irregular thin interface have been extensively studied in the last few decades, both theoretically and experimentally (see e.g. Brown and Roshko 1974; Dahm and Dimotakis 1987; Ferre et al. 1990; Mungal et al. 1991; Dimotakis 2000; Westerweel et al. 2005; Mathew and Basu 2002; Corrsin and Kistler 1955; Phillips 1955, Holzner et al. 2007 and Holzner et al. 2008). Generally, there are two proposed models for entrainment: 1) Large-scale eddy motion, "engulfing" which has been proposed by Brown and Roshko (1974), and 2) small-scale eddy, "nibbling", (Corrsin and Kistler 1955), where the latter was recently shown to dominate (Westerweel et al. 2005; Mathew and Basu 2002).

The "nibbling" phenomena is a small-scale effect and therefore its study is well suited to considering invariants of the velocity gradient tensor (VGT) to investigate the topology of the small scales at and around the interface. This was done recently by Da Silva et al (2008) using DNS of a plane jet. Here we perform a similar investigation experimentally for a round jet.

In the present study, our aim is to investigate the entrainment process formed between the non-turbulent flow and the fully turbulent flow region by the means of the invariants of the VGT. A mapping from the three dimensional flow fields to the two dimensional invariants plane can be used to analyze information relating to the dissipation of kinetic energy in the small scales and the amplification of vorticity due to vortex stretching (Martin et al. 1998; Ooi et al. 1999). The study of the invariants is well established in several flow configurations such as isotropic turbulence (Martin

et al. 1998, Nomura et al. 1998 and Ooi et al. 1999), turbulent mixing layers (Soria et al. 1994) and turbulent channel flows (Blackburn et al. 1996). Here, the variation of several "universal" features of turbulent round jets across the turbulent-non turbulent interface in the self-similar turbulent region is investigated.

The study of the invariants of the VGT requires detailed knowledge of a fully resolved three dimensional velocity field. A literature survey shows that although DNS has been the main source of velocity gradient information, the quality of experimental data of the three dimensional velocity field has been improved substantially over the last two decades, (see Maas et al. 1993 a, b; Kahler 2004; Ganapathisubramani et al. 2005; Hu et al. 2001 and Mullin et al. 2006). Two dimensional planar PIV gives just four components of the velocity gradient tensor and only one component of the vorticity vector. Stereoscopic PIV and scanning PIV can resolve the third velocity component resulting in two more components of velocity gradient information. All nine components of the velocity gradient tensor can be obtained by performing dual-plane stereoscopic PIV (DSPIV), (see Kahler 2004; Ganapathisubramani et al. 2005; Hu et al. 2001; Mullin et al. 2006) in which complete velocity gradient information can be obtained on a plane. Holographic particle image velocimetry (HPIV) is a technique with a complex setup, which can provide complete 3D velocity fields and can be utilized to compute the complete velocity gradient tensor over a volume (see Meng et al. 1995; Zhang et al. 1997; Scherer et al. 1997 and Barnhart et al. 1994). Su & Dahm (1996) introduce a new technique, Scalar Image Velocimetry (SIV), which is based on imaging the three-dimensional conserved scalar field with laser-induced fluorescence and inverting the conserved scalar transport equation to obtain all three velocity components. However, this technique requires smoothness and continuity constraints in the inversion process to obtain velocity field data (Ganapathisubramani et al. 2007).

Recently, Elsinga (2006) described the tomographic particle image velocimetry technique (Tomo-PIV) that is capable of measuring all three velocity components and the vorticity vector in a volume of a three-dimensional flow field. In this method, several simultaneous views of the illuminated particles are used to reconstruct the light intensity distribution by means of optical tomography. These reconstructive techniques are also outlined by Atkinson & Soria (2009); Worth & Nickels (2008). In this study, the Tomo-PIV technique is used to measure three components of velocity as well as all nine components of velocity gradient tensor in a turbulent round jet at Re≈3000. These data are used to compute the invariants of the velocity gradient, rate of strain and rate of rotation tensors across the T/NT interface of the jet.

2. Invariants of velocity gradient, rate of strain and rate of rotation tensors

An extensive review of the definitions of the invariants of the velocity gradient tensor can be found in the paper by Soria et al. (1994). The interpretation of these invariants, defined by their relation to the physical properties of the flow, has been studied by Chong et al. (1990); Ooi et al. (1999); Da-Silva et al. (2008), among others. In the present study, the joint probability density function (jpdf) of the invariants has been used to analyze the entrainment mechanism along the T/NT interface of a round jet. The velocity gradient tensor, $A_{ij} = \frac{\partial u_i}{\partial x_j}$, can be decomposed into a symmetric (rate-of- train) and a skew-symmetric (rate-of-rotation) component, $A_{ij}=S_{ij}+W_{ij}$, and has the following characteristic equation;

$$\lambda_i^{\,3} + P\lambda_i^{\,2} + Q\lambda_i + R = 0 . \qquad (1)$$

Here λ_i are the eigenvalues of A_{ij}, and P, Q and R are the first, second, and third invariants of the velocity gradient tensor respectively. For incompressible flows it then follows that $P=0$ due to

continuity. Similarly, the invariants of the rate-of-strain, (R_s,Q_s), and rate of rotation, (R_w,Q_w), tensors are defined by their characteristic equation, which is the same as equation 1. Jpdfs of the invariants will give physical interpretations of the flow field. The most common combination jpdfs are that of (R,Q), (R_s,Q_s) and (Q_s,Q_w).

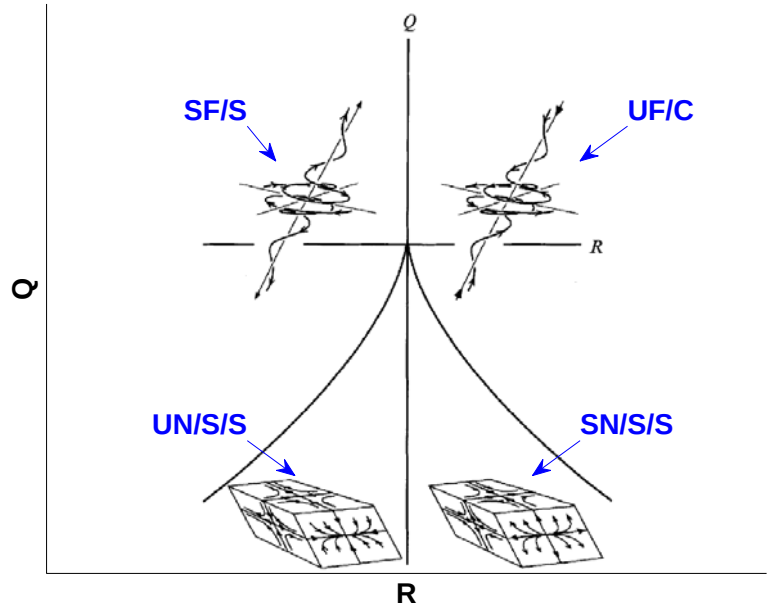

Fig. 1 Local flow fields (streamlines) for an observer travelling with the fluid for the topological classifications: upper left, stable focus/stretching ; upper right, unstable focus/compressing ; lower left, stable node/saddle/saddle; lower right, unstable node/saddle/saddle, Soria et al. (1994).

As mentioned before, the local topology of the flow field can be analyzed by two scalar quantities (second and third invariants of VGT). Typical local flow patterns are shown in figure 1. The map is divided into two different areas by the discriminant line, $D=0$ where $D = 27R^2 + 4Q^3$.

For $D<0$, the characteristic equation (eq.1) has three real roots, and if $D>0$ the characteristic equation has two complex and one real root. Furthermore, according to Chong et al. 1990, the local flow patterns which fall into the upper region are termed stable-focus-stretching (*SF/S*) if $R<0$, and unstable-focus-contracting (*UF/C*) for $R > 0$. In regions of the flow field with $D<0$ points which has $R<0$ are called stable-node/saddle/saddle while regions of the flow field with $R>0$ are termed unstable-node/saddle/saddle $R > 0$ (*UN/S/S*).

Figure 2-a shows the (Q_s,Q_w) plane. The region near the vertical axis, $Q_w=0$, indicates points in the flow with high density of dissipation of kinetic energy with little enstrophy, and the region near the horizontal axis, $Q_s=0$, represents points with high enstrophy without effect of dissipation (vortex-tubes). The (R_s,Q_s) plane is shown in figure 2-b. Since S_{ij} is a symmetric matrix (with only real eigenvalues), all the data points fall below the discriminant line and tend to be skewed toward the right hand side of the graph $R_s>0$ (two positive eigen values), indicating a predominance of sheet structures (Blackburn 1996). For $\alpha > \beta > \gamma$, where α, β, γ are the eigenvalues of rate of strain tensor, the different curves in figure 2-b correspond to the ratio of eigenvalues (e.g. 1:1:-2 equal to $\alpha : \beta : \gamma$). The most probable geometry observed in several turbulent flows corresponds to a ratio of 3:1:-4 or 2:1:-3 (Ashurst et al. 1987).

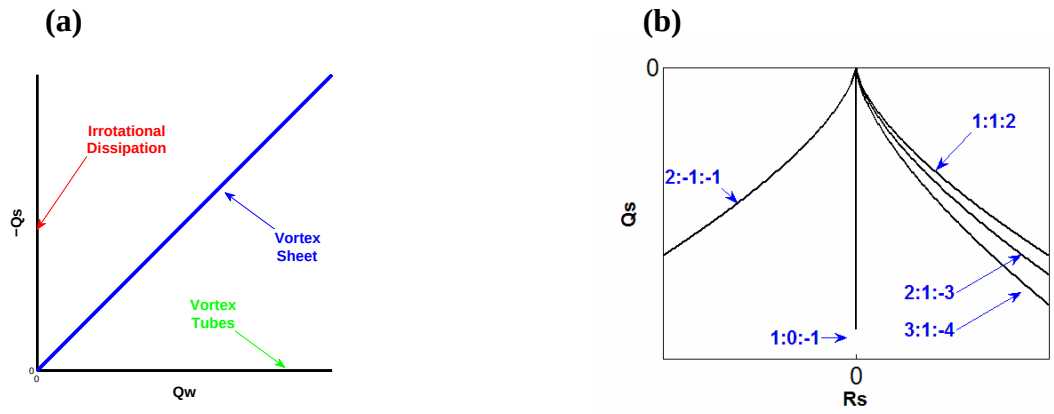

Fig. 2 Sketch of the invariant maps of rate of strain and rate of rotation tensors. a) $-Q_s$ vs Q_w with the physical/topological features of each zone and b) R_s vs Q_s -space corresponding to different ratios of eigenvalues of rate of strain tensor

3. Experimental setup

Tomo-PIV has been applied to the turbulent region of an axi-symmetric air jet to find 3D velocity distribution along the turbulent-nonturbulent interface, while a 2D planar PIV measurement was used for the measurement of streamwise and spanwise components to document the jet conditions and validate the statistical results of the Tomo-PIV.

The experimental setup consists of a 2 mm diameter nozzle fixed to a machined plate that is bolted on linear bearings attached to a vertical rail, allowing accurate positioning of the jet exit in the vertical direction. A schematic diagram is shown in figure 3. The mean velocity of the flow at the jet exit was 23m/s, indicating *Re=3000*. The seeding material used was a water-based sugar solution containing 12 g/L of sugar. This solution is vaporized by eight Ultrasound devices (*APC Nebuliser*) which were operated in a cylindrical container and produced water droplets with an average 2μm diameter. In addition, a separate particle generator was used to seed the air outside the jet to create enough particle density in the shear layer and non-turbulent region. Due to non homogeneity of this type of seeding, after seeding some time was allowed for the background flow to settle and for the seeding to become homogeneous.

For the Tomo-PIV experiments 4 *PCO4000* cameras were used and were positioned such that all 4 cameras operated in forward scatter with X-95 rails used to mount 2 cameras looking at an angle of 10^o down on the jet, while the other 2 cameras looked at the same angle upwards towards the jet. All cameras were at an angle of 25^o from the angle perpendicular to the direction of the light sheet (Fig.3). The cameras have a spatial resolution of 4008×2670 pixels and a framing rate of 2 Hz in double frame operating condition. Four 200 mm Nikon lenses were fitted to the cameras, which can provide magnification of 0.91, and the field of view of 38×28 mm^2.

Illumination of the particles was provided by a twin-cavity frequency, double pulsed Nd:YAG laser (*Big Sky)* that emits at the 512nm wavelength that provided a 1mm thick light sheet for planar PIV and 3 mm tick for Tomo-PIV experiments, which corresponded to the depth of view of the cameras at $f^{\#}$=16. The δt value used for the laser pulses was 0.01ms, which corresponds to the one quarter law for the in-plane displacement (Kean and Adrian 1992) in the center of the images.

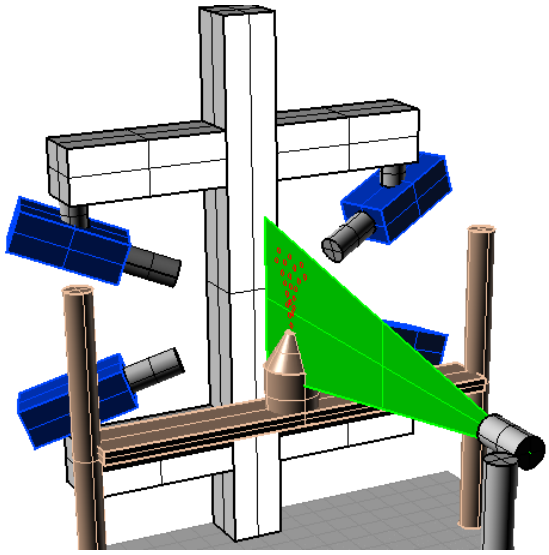

Fig. 3 Schematic diagram of the jet experiment setup

In order to have uniform background seeding in the outer flow, in addition to the seeded jet a tent was placed over the setup to confine the seeding particles. This background seeding was required to measure the velocity in the entrainment region of the flow.
The camera calibration device was mounted on bearings that fitted onto the same rails as the jet giving it vertical movement and was mounted on a micrometer allowing horizontal motion. The calibration grid itself was a white transparency with black dots spaced at a distance of 2.5 mm that was used in order to place all cameras in forward scatter.
All the cameras were operated in double frame and were synchronized with the lasers in order to record the light which was scattered by the tracer particles. Images were collected at a rate of 2 Hz, which is corresponds with the maximum frame rate of *PCO4000* at double frame mode. Due to the limitation of the number of images in each experiment (memory limitation), each experiment was repeated to obtain sufficient images (500 images for Tomo-PIV and 1100 images for Planar PIV). The recorded particle images were analyzed using the DaVis software from LaVision GmbH. The 3-D intensity distribution was reconstructed using the MART algorithm with 5 iterations, (Elsinga et al. 2006), at a spatial resolution of 100 *voxels/mm*. The volume frame pairs were interrogated with $44 \times 44 \times 44$ interrogation volume size with 50 percent overlap. Each volume yielded $153 \times 76 \times 22$ (404000) velocity vectors with a spatial resolution of 0.4 mm. Figure 4 shows an example of the instantaneous velocity field obtained by Tomo-PIV.

4. Turbulent velocity and scalar statistics

In this paper, *x*, *y* and *z* are the stream-wise, span-wise and laser-sheet normal axes, with *u*, *v* and *w* denoting the respective fluctuating velocity components. Using the large data set acquired with Tomo-PIV, it is possible to investigate all three components of velocity and vorticity vectors as well as nine components of VGT. The result for the mean centerline velocity, *U*, turbulence intensity of all velocity components and Reynolds shear stress, $< uv >$, are shown in Fig. 5. In all graphs, velocity magnitudes are normalized by U_c where U_c is the maximum centerline of U and the radius is normalized by d, the local half-width of the mean velocity profile. 2D-2C PIV measurements have been performed to validate the statistical result of Tomo-PIV. This experimental finding is in agreement with results obtained by others, e.g. Hussain et al. (1998), Da

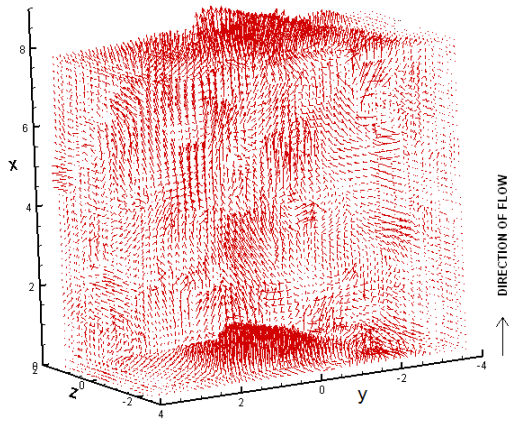

Fig. 4 Example of the instantaneous velocity field obtained by the Tomo-PIV

Silva et al. (2008). The presented profiles were taken at *X/D=20*, which is in the self-similar region. Figure 5 shows the result of one point statistics in a self-similar turbulent round jet. The streamwise mean velocity profile is shown in figure 5(a), and is in good agreement with the result of previous work, (see e. g. Matsuda et al. 2005, Da Silva et al. 2008). The streamwise turbulent intensity in figure 5(b) also shows reasonable agreement using Planar PIV results, although the *RMS* value of *u* appear to be lower in the center of the jet when compared with the Planar-PIV data. The *RMS* of the second and third components of velocity (*v* and *w*, respectively), is shown in figure 5(c). These results agree well with the planar PIV data and other previous work. Figure 5(d) shows the Reynolds shear stress $\langle uv \rangle$ normalized by U_c^2, where $\langle\rangle$ denotes the streamwise average and the ensemble average.

5. Result

5.1 Accuracy of Tomo-PIV measurements

A brief discussion of the accuracy of the computed velocity gradient is presented in this section. Following Ganapathisubramani (2007), the quality of the result of velocity gradients can be evaluated by comparing some quantities of the velocity gradient with isotropic conditions. For example, an isotropic condition implies that the following ratios, $\overline{[\frac{\partial u}{\partial y}]^2} \Big/ \overline{[\frac{\partial u}{\partial z}]^2}$, $\overline{[\frac{\partial v}{\partial x}]^2} \Big/ \overline{[\frac{\partial w}{\partial x}]^2}$, $\overline{[\frac{\partial v}{\partial y}]^2} \Big/ \overline{[\frac{\partial w}{\partial z}]^2}$ and $\overline{[\frac{\partial v}{\partial z}]^2} \Big/ \overline{[\frac{\partial w}{\partial y}]^2}$, should all be equal to 1**.** The measured values of isotropic ratios for Tomo-PIV results are 0.9312, 1.052, 0.8517 and 0.8312 respectively. These results show at least a 15 percent variation from the isotropic condition. These results are very similar with the result of Ganapathisubramani et al. (2007) where the values of ratios indicate 10 percent disparity from the isotropic condition.

The accuracy of the computed velocity gradients can also be evaluated by measuring the divergence error. If the continuity equation is satisfied, the values of $\nabla \cdot U$ for each data point should be equal to zero. Figure 6 shows the pdf of divergence error relative to the velocity gradient norm. This distribution has the mean value of zero and the RMS equal to 0.3, which is very similar to the result of cinematographic stereoscopic PIV by Ganapathisubramani et al. (2007) and dual-plane stereoscopic PIV measurements by Mullin et al. (2006).

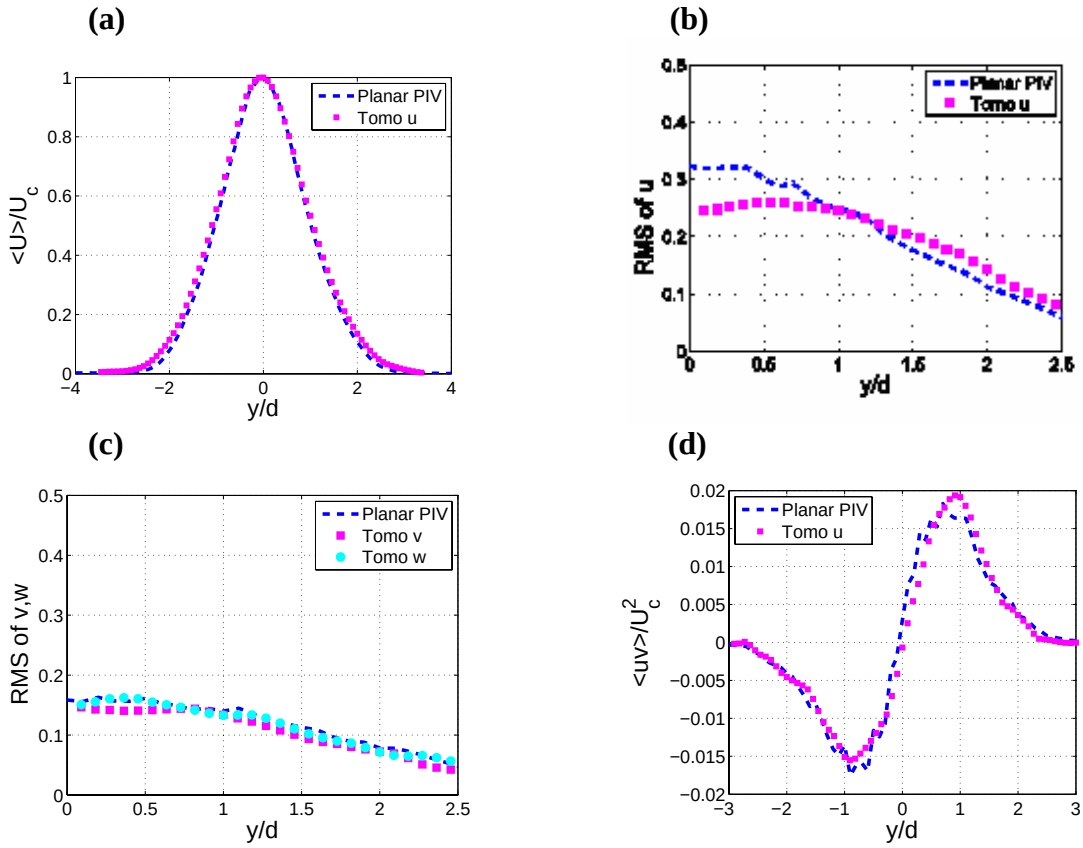

Fig. 5 Profiles of several one point statistics at the self-similar region from the present Tomo-PIV result compared with the planar PIV and the experimental results from da silva et al. (2008). a) Mean stream-wise velocity profile, b) stream-wise RMS, c) Spanwise and sheet-normal RMS and d) Reynolds shear stress. U_c is the stream-wise mean centerline velocity and d is the half-width of the jet.

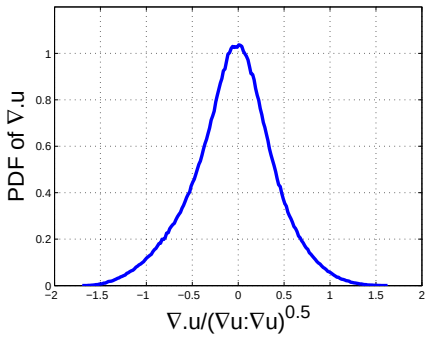

Fig. 6 pdf of divergence error elative to the norm of the velocity gradients

Based on the above discussion, the effect of the divergence error on the intrinsic uncertainty of the Tomo-PIV result can be seen. Note that intrinsic Tomo-PIV uncertainty includes errors in geometric distortion, peak detection error in three dimensional cross correlation, reconstruction quality (existence of ghost particles), spatial resolution and experimental setup (misalignment of the laser-sheets). Moreover, the velocity gradient measurements using the central difference scheme can be another source of the divergence error.

5.2 Detection of T/NT interface

The T/NT interface can be detected by the vorticity criteria, which was first introduced by Bisset et al. (1998). This interface can also be detected by velocity criteria (Holzner et al. 2006), concentration criteria (Prasad and Sreenivasan 1989) and velocity-vorticity criteria (Anand et al. 2009). The vorticity criteria was used in the present work, where a ratio of the total vorticity magnitude and maximum vorticity value (ω_t/ω_0) with respect to a threshold value is used, to detect the interface. The fluid is in the turbulent region if the ratio ω_t/ω_0 is greater than the threshold value and in the non-turbulent region if ω_t/ω_0 is less than the threshold value. A threshold of 0.1 is used for the result presented in this work.
After determination of the interface, a new coordinate is defined (y_i) where its origin is located in the interface, and conditional statistics in relation to the new coordinate can be found by using a procedure similar to the one described in Bisset et al. (2002) and Westerweel et al. (2005).
For each data point inside the flow volume, the three dimensional velocity field is used to compute the conditional invariants of the velocity gradient as well as the rate of strain and rate of rotation tensors. Jpdf of conditional values of (R,Q), (R_s,Q_s) and (Q_w,Q_s) for three different locations: $(y-y_i)/d=0$ (interface), $(y-y_i)/d=0.5$ (maximum of $<\omega_z>$) and $(y-y_i)/d=2$ (turbulent region) are plotted in figures 8-10. A detailed comparison for each graph is also elaborated in the following sections.

5.3 Analysis of the jpdfs of (Q_w, Q_s), (R_s, Q_s) and (R, Q)

In the previous section, we investigated the way of detecting the interface by means of vorticity criteria and assuming that all the values of vorticity bigger than the threshold values are located inside the turbulent region and the rest are located in the irrotational region. The conditional investigation of the invariants of the velocity gradient, rate of strain and rate of rotation tensors have been measured by the new coordinate, y_i. Figure 7 shows the mean conditional values of the invariants $<Q_w>$, $<Q_s>$ and $<R_s>$ with the mean values of $<\omega_z>$ along the T/NT interface.

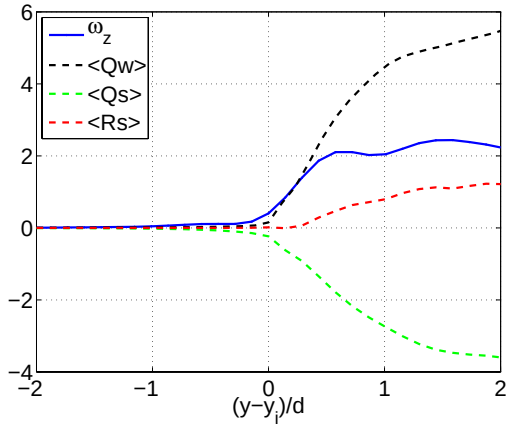

Fig. 7 Mean conditional profiles of $<Q_w>$, $<Q_s>$, $<R_s>$ and $<\omega_z>$ along the T/NT interface

As can be seen clearly from figure 7, the value of all the invariants is close to zero in the irrotational region and increases quite suddenly at the interface, $(y-y_i)/d=0$. Another observation is that the absolute value of $<Q_s>$ starts to increase from the irrotational region, at approximately $(y-y_i)/d=-0.7$ onward and its magnitude at the interface is found to be -0.75. The value of Q_s is proportional to

the rate of dissipation of kinetic energy and a non-zero value of Q_s in the irrotational region indicates the existence of viscous dissipation. This result is consistent with the existence of irrotational velocity fluctuations and Reynolds stresses in the near of the interface (Westerweel et al. 2005).

Figure 7 also shows that the rate of change of $<Q_s>$ after the interface is higher than it was before the interface but this rate is smaller than the $<Q_w>$ after the interface. On the other hand, $<Q_s>$ needs more time to reach its turbulent value than enstrophy (Da Silva et al. 2008).

Iso-contour of jpdf of second invariants of rate of strain and rate of rotation tensors, $-Q_s$ and Q_w respectively, for three different location from the interface, $(y-y_i)/d=0$, $(y-y_i)/d=0.5$ and $(y-y_i)/d=2$ are plotted in figure 8. The invariants are normalized with the $<Q_w>$, where $<Q_w>$ is taken for each interface location. As expected, at the interface, $(y-y_i)/d=0$, jpdf shows a high tendency toward the Q_s where the dissipation dominates enstrophy. In location $(y-y_i)/d=0.5$ where the turbulence is intensified and value of $<\omega_z>$ reaches its maximum value, the jpdf changes its shape and flow topology detaches from the vertical line and approaches the 45^o line. Further away from the interface, $(y-y_i)/d=2$, the data points of $-Q_s$ and Q_w tend to keep their correlation in the topology map with a slight tendency toward the axis Q_s=0. Thiese results show good agreement with the results of the jpdf of isotropic turbulence (Ooi et al. 1999) and turbulent channel flow (Blackburn et al. 1996).

Figure 9 shows the jpdf of the invariants R_s and Q_s in the three different locations mentioned previously. The apparent excursions above this region that can be seen in figure 9 are the result of non-zero value of the divergence. The contour levels shown are the same as those used for the jpdf

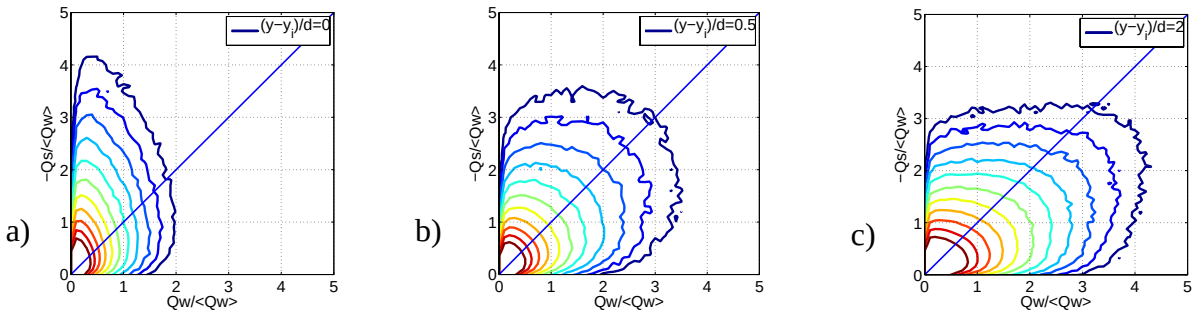

Fig. 8 jpdfs of Q_s and Q_w at three conditional locations: a) $(y-y_i)/d=0$, b) $(y-y_i)/d=0.5$ and c) $(y-y_i)/d=2$

distributions presented for Q_s and Q_w. As mentioned, the symmetry of S_{ij} forces the data to fall below the discriminant line $D_s=0$. Deviations above here are due to noise and error resulting in a non zero divergence for velocity. The color dashed lines in the graph show the regions where the eigenvalues of the rate of strain tensor has the ratio $\alpha:\beta:\gamma$, (black line (1:1:-2), green line (2:1:-3) and red line (3:1:-4)). The graphs may not appear to have any fundamental difference but the average of the eigenvalues of the rate of strain tensor for the three areas show that the eigenvalues in the interface, $(y-y_i)/d=0$, have the ratio of $3:1:-3.8$, for the $(y-y_i)/d=0.5$, this ratio is $2.6:1:-3.2$ and in the turbulent region is found to be $2.6:1:-3.6$. Figure 9 also shows the tendency of the contour lines toward the right hand side of the discriminant line.

The behavior of the jpdf of R and Q is shown in figure 10. Since there is no vorticity in the irrotational region outside the jet, the value of Q, which is proportional to the vorticity magnitude for $Q>0$, should be negative and all the data points in this region ($(y-y_i)/d=0$) are expected to fall below the discriminant line. At two other location, $(y-y_i)/d=0.5$ and $(y-y_i)/d=2$, the jpdf of R and Q shows the universal features of the turbulence ("tear drop" shape), where the contour lines tend to be skewed toward the second and fourth quadrant of the map: $R>0$, $Q<0$

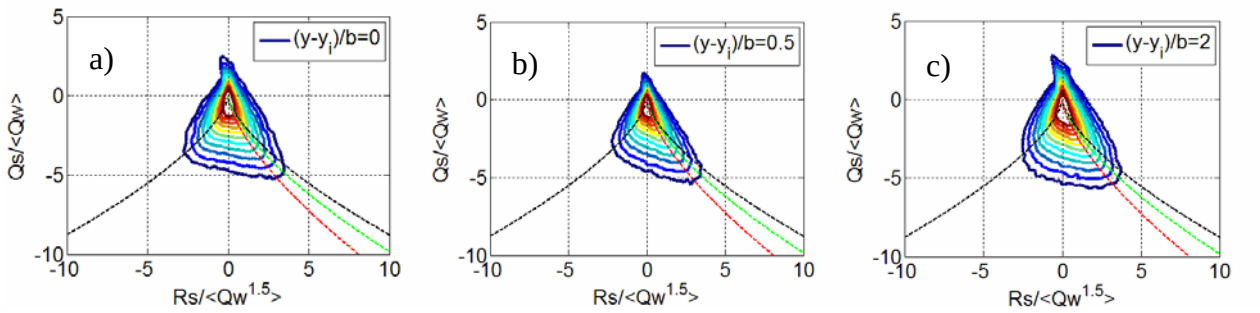

Fig. 9 jpdfs of Q_s and R_s at three conditional locations: a) $(y-y_i)/d = 0$, b) $(y-y_i)/d = 0.5$ and c) $(y-y_i)/d = 2$

representing *SN/S/S* and $R<0$, $Q>0$, `which is proportional to the SF/S. Note that the shape of the jpdfs in figure 10-b and 10-c is very similar and has a good agreement with the results of planar jet (Da Silva et al. 2008), isotropic turbulence (Ooi et al. 1999), turbulent channel flow (Blackburn et al. 1996) and turbulent boundary layers (Chong et al 1998, Elsinga and Marusic 2010).

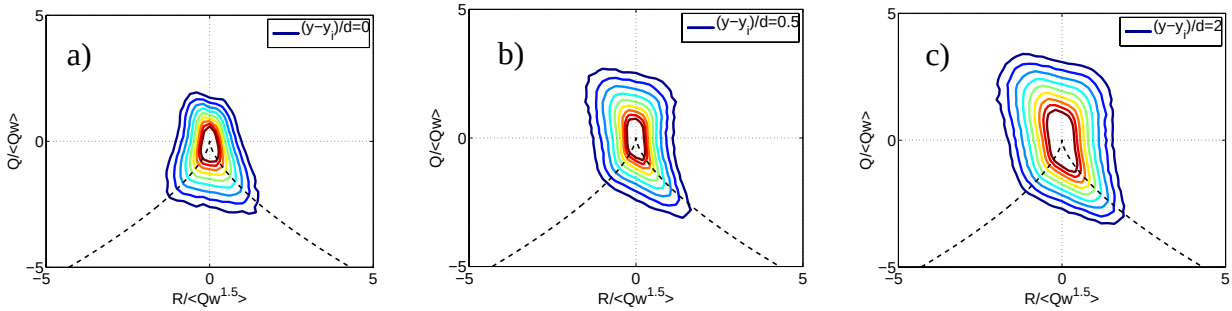

Fig. 10 jpdfs of Q and R at three conditional locations: a) $(y-y_i)/d = 0$, b) $(y-y_i)/d = 0.5$ and c) $(y-y_i)/d = 2$

6. Conclusions

Tomo-PIV measurements were made on a three dimensional round jet along the T/NT interface at *Re=3000*. Consequently, the study of invariants of velocity gradient, rate of strain and rate of rotation tensors are reported from which dynamics and topology of the flow in this area of interest have been investigated. The Tomo-PIV measurements have been found to be useful for studying invariants of the VGT with accuracy similar to those acheaved by cinematographic stereoscopic PIV (Ganapathisubramani et al. 2007) and dual-plane stereoscopic PIV (Mullin et al. 2006).

The most interesting outcome of this study is that the average value of all the invariants is zero in the outer region (irrotational) and jpdf of all invariants at the turbulent region show the universality pattern (a tear-drop shape) which has been shown in previous studies.

The jpdf of R vs Q shows that in the irrotational region, most focal regions in the flow tend to be aligned around the $R<0$ line in the $Q<0$ area. As the interface is passed, stretching of vortex lines occurs and most focal regions in the flow have local topology SF/S, which is consistent with previous studies. The jpdf of Q_s and R_s show a skewed behavior biased to the $R_s>0$ side, which implies that the mean flow geometry is already characterized by the straining of the fluid elements.

Visualizations of contours of Q_s and Q_w show that the contour lines tend to be attached to the Q_s axis in the interface and scattered in the whole first quadrant of the graph with a little tendency toward the Q_w axis, away from the interface. This graph is very similar to the ones observed in isotropic turbulence by Ooi et al. (1999).

7. Acknowledgements

The support of the Australian Research Council is gratefully acknowledged.

8. References

Anand RK, Boersma BJ, Agrawal A (2009) Detection of turbulent/non-turbulent interface for an axisymmetric turbulent jet: evaluation of known criteria and proposal of a new criterion. Exp Fluids 47:995-1007

Ashurst W, Kerstein A, Kerr R, Gibson C (1987) Alignment of vorticity and scalar gradient with strain rate in simulated Navier-Stokes turbulence. Phys Fluids 30:2343

Atkinson C, Soria J (2009) An efficient simultaneous reconstruction technique for tomographic particle image velocimetry. Exp Fluids 47:553–568.

Barnhart DH, Adrian RJ, Meinhart CD, Papen GC (1994) Phaseconjugate holographic system for high resolution particle image velocimetry. Appl Opt 33:7159–7169

Bisset DK, Hunt JCR, Rogers MM (2002) The turbulent/non-turbulent interface bounding a far wake. J Fluid Mech 451:383–410

Blackburn H, Mansour N, Cantwell B (1996) Topology of fine-scale motions in turbulent channel flow. J Fluid Mech 310:269

Brown GL, Roshko A (1974) On density effects and large structure in turbulent mixing layers. J Fluid Mech 64:775–816

Chong MS, Perry E, Cantwell B (1990) A general classification of three dimensional flow fields simulations of turbulence. Phys Fluids A 2:765

Chong MS, Soria J, Perry E, Chacin J, Cantwell B, Na Y (1998) A study of the turbulence structures of wall-bounded shear flows using DNS data. J Fluid Mech 357: 225

Corrsin S, Kistler AL (1954) The free-stream boundaries of turbulent flows. NACA TN-3133, TR-1244: 1033–1064

Dahm WJA, Dimotakis PE (1987) Measurements of entrainment and mixing in turbulent jets. AIAA J 25:1216–1223

Da Silva BC, Pereira JCF (2008) Invariants of the velocity-gradient, rate-of-strain, and rate-of-rotation tensors across the turbulent/ nonturbulent interface in jets. Phys Fluids 20:055101

Dimotakis PE (2000) The mixing transition in turbulent flows. J Fluid Mech 409:69–98

Elsinga GE, Scarano F, Wieneke B, van Oudheusden BW (2006) Tomographic particle image velocimetry. Exp Fluids 41(6):933– 947

Elsinga GE, Marusic I (2010) Evolution and lifetimes of flow topology in a turbulent boundary layer. Phys Fluids 22:015102

Ferre JA, Mumford JC, Savill AM, Giralt F (1990) Three-dimensional largeeddy motions and fine-scale activity in a plane turbulent wake. J Fluid Mech 210:371–414

Ganapathisubramani B, Longmire EK, Marusic I, Pothos S (2005) Dual-plane PIV technique to measure complete velocity gradient tensor in a turbulent boundary layer. Exp Fluids 39(2):222–231

Ganapathisubramani B, Lakshminarasimhan K (2007) Determination of complete velocity gradient tensor by using cinematographic stereoscopic PIV in a turbulent jet. Exp Fluids 42: 923–939.

Holzner M, Liberzon A, Gaula M, Tsinober A (2006) Generalized detection of a turbulent front generated by an oscillating grid. Exp Fluids 41:711–719

Holzner M, Liberzon A, Nikitin N, Kinzelbach W, Tsinober A (2007) Small-scale aspects of flows in proximity of the turbulent/nonturbulent Interface. Phys Fluids 19: 071702

Holzner M, Liberzon A, Nikitin N, Luthi B, Kinzelbach W, Tsinober A (2008) A Lagrangian investigation of the small-scale features of turbulent entrainment through particle tracking and direct numerical simulation. J Fluid Mech, 598: 465–475

Hu H, Saga T, Kobayashi T, Taniguchi N, Yasuki M (2001) Dualplane stereoscopic particle image velocimetry: system set-up and its application on a lobed jet mixing flow. Exp Fluids 31:277–293

Hussain HJA (1998) Selection of Test Cases for the Validation of Large-Eddy Simulations of Turbulent Flows,AGARD ADVISORY REPORT 345

Ka¨hler CJ (2004) Investigation of the spatio-temporal flow structure in the buffer region of a turbulent boundary layer by means of multiple plane stereo PIV. Exp Fluids 36:114–130

Keane RD, Adrian RJ (1992) Theory of cross-correlation analysis of PIV images. Appl Sci Res 49:191

Maas HG, Gruen A, Papantoniou D (1993a) Particle tracking in three dimensional turbulent flows—part I: Photogrammetric determination of particle coordinates. Exp Fluids 15:133–146

Maas HG, Gruen A, Papantoniou D (1993b) Particle tracking in three dimensional turbulent flows—part II: Particle tracking. Exp Fluids 15:279–294

Martin J, Ooi A, Chong MS, Soria J (1998) Dynamics of the velocity gradient tensor invariants in isotropic turbulence. Fhys Fluids A 10: 2336.

Mathew J, Basu AJ (2002) Some characteristics of entrainment at a cylindrical turbulence boundary. Phys Fluids 14:2065–2072

Matsuda T, Sakakibara J (2005) On the vortical structure in a round jet. Phys Fluids 17-025106:1–11

Meng H, Hussain F (1995) Instantaneous flow field in an unstable vortex ring measured by HPIV. Phys Fluids 7:9–11

Mullin JA, Dahm WJA (2006) Dual-plane stereo particle image velocimetry measurements of velocity gradient tensor fields in turbulent shear flow. I. Accuracy assessments. Phys Fluids 18- 035101:1–18

Mungal MG, Karasso PS, Lozano A (1991) The visible structure of turbulent jet diffusion flames: large-scale organization and flame tip oscillation. Combust Sci Technol 76:165–185

Nomura K, Post G (1998) The structure and dynamics of vorticity and rate of strain in incompressible homogeneous turbulence . J Fluid Mech 377: 65

Ooi A, Martin J, Soria J, Chong MS (1999) A study of the evolution and characteristics of the invariants of the velocity-gradient tensor in isotropic turbulence. J Fluid Mech 381:141

Phillips OM (1955) The irrotational motion outside a free boundary layer. Proc Camb Phil Soc 51:220

Prasad RR, Sreenivasan KR (1989) Scalar interfaces in digital images of turbulent flows. Exp Fluids 7:259–264

Scherer JO, Bernal LP (1997) In-line holographic particle image velocimetry for turbulent flows. Appl Opt 36:9309–9318

Soria J, Sondergaard R, Cantwell B, Chong MS, Perry A (1994) A study of the fine-scale motions of incompressible time-developing mixing layers. Phys. Fluids A 6:871

Su LK, Dahm WJA (1996) Scalar imaging velocimetry measurements of the velocity gradient tensor field in turbulent flows. II. Experimental results. Phys Fluids 8:507–521

Westerweel J, Fukushima C, Pedersen JM, Hunt JCR (2005) Mechanics of turbulent-non-turbulent interface of a jet. Phys Rev Lett 95:174501

Worth NA, Nickels TB (2008) Acceleration of Tomo-PIV by estimating the initial volume intensity distribution. Exp Fluids 45: 847–856.

Zhang J, Tao B, Katz J (1997) Turbulent flow measurement in a square duct with hybrid holographic PIV. Exp Fluids 23:373– 381